Available online at www.sciencedirect.com
SCIENCE DIRECT®
Journal of Sound and Vibration 291 (2006) 861–881
JOURNAL OF SOUND AND VIBRATION
www.elsevier.com/locate/jsvi

Bifurcation analysis of an automatic dynamic balancing mechanism for eccentric rotors

K. Green[a,*], A.R. Champneys[a], N.J. Lieven[b]

[a]*Bristol Laboratory for Advanced Dynamics Engineering, Department of Engineering Mathematics, University of Bristol, Queen's Building, University Walk, Bristol BS8 1TR, UK*
[b]*Department of Aerospace Engineering, University of Bristol, Queen's Building, University Walk, Bristol BS8 1TR, UK*

Received 9 July 2004; received in revised form 25 February 2005; accepted 30 June 2005
Available online 17 November 2005

Abstract

We present a nonlinear bifurcation analysis of the dynamics of an automatic dynamic balancing mechanism for rotating machines. The principle of operation is to deploy two or more masses that are free to travel around a race at a fixed distance from the hub and, subsequently, balance any eccentricity in the rotor. Mathematically, we start from a Lagrangian description of the system. It is then shown how under isotropic conditions a change of coordinates into a rotating frame turns the problem into a regular autonomous dynamical system, amenable to a full nonlinear bifurcation analysis. Using numerical continuation techniques, curves are traced of steady states, limit cycles and their bifurcations as parameters are varied. These results are augmented by simulations of the system trajectories in phase space. Taking the case of a balancer with two free masses, broad trends are revealed on the existence of a stable, dynamically balanced steady-state solution for specific rotation speeds and eccentricities. However, the analysis also reveals other potentially attracting states—non-trivial steady states, limit cycles, and chaotic motion—which are not in balance. The transient effects which lead to these competing states, which in some cases coexist, are investigated.

1. Introduction

Vibrations in rotating machinery are predominantly caused by an eccentric imbalance. If the system has a fixed imbalance it is easy to balance using additional static masses. However, in a number of cases, the position of the imbalance may be free to vary in time. Therefore, it is hard to predict, a priori, where and when the imbalance will occur. This observation motivates the use of self-compensating, automatic dynamic balancers (ADB), that is, passively controlled balancing devices that require no external forces to achieve balance.

The use of ADBs would be advantageous in a number of physical applications; for example, the balancing of optical disc drives to obtain higher operating speeds without a drop in the tracking performance [1–4], and the balancing of machine tools, such as, lathes, angle grinders and cutting tools [5]. By preventing vibrations and subsequently stress, the use of an ADB may lengthen the life-time of operation of such devices. In

*Corresponding author. Present address: Theoretical Physics, FEW, Vrije Universiteit, De Boelenlaan 1081, 1081 HV Amsterdam, The Netherlands.
E-mail address: kirk.green@bristol.ac.uk (K. Green).

0022-460X/$ - see front matter © 2005 Elsevier Ltd. All rights reserved.
doi:10.1016/j.jsv.2005.06.042

particular, using an ADB for decreasing vibration in machine tools is of great economical value as a balanced machine can be operated for more sustained periods of time by a single worker, without the threat of health problems such as 'Hand-arm vibration syndrome' (HAVS) [6].

A review of the early history of ADBs is included in the study by Lee and Van Moorhem [7]. The first ADB was proposed as early as 1904 with the first theoretical study conducted by Thearle in 1932 [8]. Since then there has been great interest in manufacturing ADBs, with a number of patents granted from 1961 onwards [7]. The key idea of an ADB is to deploy two or more masses that are free to travel around a race, filled with a viscous fluid, at a fixed distance from the centre of rotation of the rotor; see Fig. 1 below. This simple arrangement motivated the theoretical studies by Sharp [9], Bövik and Högfors [10], and Majewski [11]. More recently, the equations of motion of the ADB were derived using Lagrange's method [7,12]. In particular, Chung and Ro [12] carried out a linear stability analysis using perturbation methods and identified stability regions of the full nonlinear problem using a scatter-gun approach. Adolfsson [13] applied a similar linear stability analysis and identified regions of stable, balanced operation by considering the largest real eigenvalue. Numerical simulation has also been employed to verify the stability of the ADB. However, due to the highly nonlinear nature of the problem, these studies have shown that the ADB mechanism may make things catastrophically worse at some parameter values [12] and, therefore, there has only been limited successful commercial application of the ADB mechanism [14]. Moreover, a linear stability analysis is an inadequate tool for understanding such nonlinear behaviour. Finally, we note that some experimental studies have been carried out to verify the validity of the mathematical models; see Refs. [2,7].

In this paper, we provide the first, detailed nonlinear bifurcation analysis of the dynamics of the ADB using numerical continuation tools [15]. Mathematically, we start from a time-dependent Lagrangian model. We then turn the problem into a time-independent (autonomous) system by considering the equations of motion in a rotating frame. This autonomous form has the advantage of being amenable to a full nonlinear bifurcation analysis. In particular, we use the continuation package AUTO [15] which allows one to find and follow steady states and periodic solutions, irrespective of their stability, and to detect local bifurcations. These bifurcations, marking the stability boundaries of the full nonlinear system, can then be followed as parameters are varied. In this way, a detailed 'map' is built-up of the stable regions of the ADB in a desired parameter space. The results obtained by continuation are reinforced using standard numerical simulation of the governing equations of motion. Furthermore, our analysis reveals unbalanced, stable limit cycle solutions

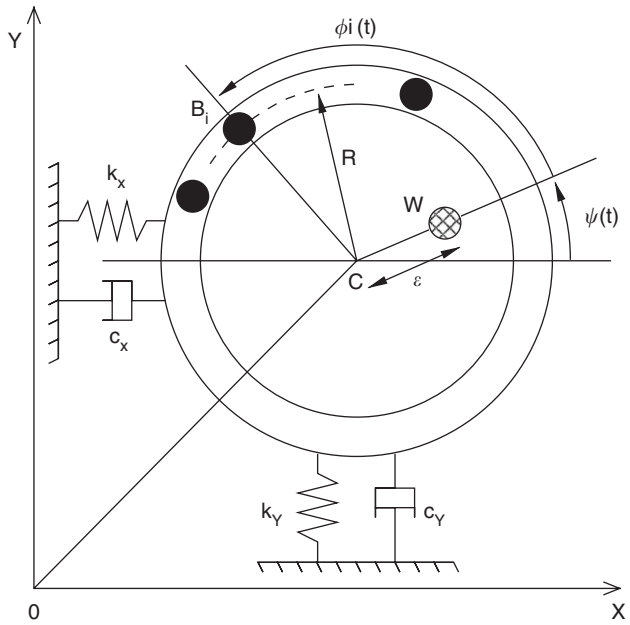

Fig. 1. Schematic diagram of an automatic dynamic balancer, see the text for definitions of the variables.

which coexist with balanced steady-state solutions. This bistability can have an adverse effect on the smooth operation of the balancer; for example, small perturbations to a balanced steady state, thought stable by a linear stability analysis, may cause imbalance as the dynamics are attracted to the periodic solution.

The paper is organised as follows. In Section 2, we derive the equations of motion for the ADB. Specifically, in Section 2.1 we formulate a Lagrangian description of the system; we then derive a dimensionless form in Section 2.2. In Section 2.3 the equations of motion are rewritten in a rotating frame of reference to produce a time-independent, autonomous form. In Section 3.1 steady-state solutions are found and various conditions governing their existence are identified. Continuation techniques are employed in Section 3.2 to investigate what effect varying physical parameters in the system has on the stability of the steady-state solutions. In Section 4 periodic solutions are found and their stability investigated. In particular, we identify bistabilities between a balanced steady-state solution and an unbalanced periodic solution. In Section 5, we investigate the transient dynamics of solutions and their sensitivity to initial conditions using numerical simulation. Finally, in Section 6 we draw conclusions and discuss future work.

2. Equations of motion

Our object of study is an eccentric rotating disc together with an ADB consisting of two or more balls free to move in a race filled with a viscous fluid and positioned at a fixed distance from the centre of rotation of the disc. This set-up is shown schematically in Fig. 1. The point W represents the centre of mass of the disc (without the balancing balls) and is located a distance ε from the centre of rotation, point C. Note that this model assumes that the disc is attached to a non-flexible shaft through the point C. For a study of an eccentric rotor with a flexible shaft see Ref. [16].

In the following section we will derive the equations of motion of an ADB using Lagrange's method, where we make the assumption that all motion is confined to the two-dimensional (X, Y)-plane. We also assume that there are no interactions between the balls. This assumption is valid provided the balls are in an equilibrium state. Note that neglecting impacts between the balls motivated the study of an ADB with double ball races, that is, assuming two balls, each ball moves in its own race [17]. The following analysis holds for either single or multiple race models, where each race is assumed to be at the same radial distance from the rotor spindle. Our analysis initially follows a Lagrangian description first considered in Ref. [7]. In addition, we develop a dimensionless model in a rotating frame; see, for example, Ref. [13].

2.1. Lagrangian description

The equations of motion describing an ADB can be derived from Lagrange's equation

$$\frac{\mathrm{d}}{\mathrm{d}t}\left(\frac{\partial T}{\partial \dot{q}_k}-\frac{\partial V}{\partial \dot{q}_k}\right)-\frac{\partial T}{\partial q_k}+\frac{\partial V}{\partial q_k}=Q_k, \tag{1}$$

where T is the kinetic energy, V is the potential energy, q_k are the generalised coordinates and Q_k are the generalised forces acting on the system. Assuming the disc moves in the (X, Y)-plane, the generalised coordinates are given as

$$\mathbf{q}=(X, Y, \psi, \phi_i), \tag{2}$$

where $\phi_i\,(i=1\ldots n)$ represents the angular position of the ith ball and ψ the angular position of the imbalance.

The position vector of the centre of mass W of the disc is

$$\mathbf{r}_{OW}=(X+\varepsilon\cos\psi)\mathbf{i}+(Y+\varepsilon\sin\psi)\mathbf{j}, \tag{3}$$

where $\mathbf{i}$ and $\mathbf{j}$ are unit vectors in the X and Y coordinate directions, respectively.

The position vector of the ith ball is

$$\mathbf{r}_{OB_i}=(X+R\cos(\psi+\phi_i))\mathbf{i}+(Y+R\sin(\psi+\phi_i))\mathbf{j}. \tag{4}$$

Moreover, the respective velocities are given as

$$\dot{\mathbf{r}}_{OW}=(\dot{X}-\varepsilon\dot{\psi}\sin\psi)\mathbf{i}+(\dot{Y}+\varepsilon\dot{\psi}\cos\psi)\mathbf{j}, \tag{5}$$

$$\dot{\mathbf{r}}_{OB_i} = (\dot{X} - R(\dot{\psi} + \dot{\phi}_i)\sin(\psi + \phi_i))\mathbf{i} + (\dot{Y} + R(\dot{\psi} + \dot{\phi}_i)\cos(\psi + \phi_i))\mathbf{j}. \tag{6}$$

The total kinetic energy of the system is given by

$$T = \frac{1}{2} I_z \dot{\psi}^2 + \frac{1}{2} M(\dot{\mathbf{r}}_{OW} \cdot \dot{\mathbf{r}}_{OW}) + \frac{1}{2} \sum_{i=1}^{n} m_i (\dot{\mathbf{r}}_{OB_i} \cdot \dot{\mathbf{r}}_{OB_i}), \tag{7}$$

where M is the mass of the disc, m_i is the mass of the ith ball and I_z is the moment of inertia of the rotor about C. The potential energy of the system is given by

$$V = \frac{1}{2} k_X X^2 + \frac{1}{2} k_Y Y^2 + MgY + \sum_{i=1}^{n} m_i g(Y + R\sin(\psi + \phi_i)), \tag{8}$$

where g is the acceleration due to gravity, and k_X and k_Y are linear spring constants acting on the rotor system in the X and Y directions, respectively.

Finally, the generalised forces, that is, forces not arising from a potential, are given by

$$\mathbf{Q} = -\frac{\partial F}{\partial \dot{q}_k} = (-c_X \dot{X}, -c_Y \dot{Y}, \tilde{M}, -D_i \dot{\phi}_i), \tag{9}$$

where F is Rayleigh's dissipation function, c_X and c_Y are linear damping constants acting on the rotor in the X and Y directions, respectively, $\tilde{M}$ is the moment driving the system, and D_i is a linear drag coefficient acting on the ith ball.

Substituting Eqs. (7)–(9) into Eq. (1) yields the nonlinear equations of motion. The first equation of motion is

$$\begin{aligned} M\ddot{X} - M\varepsilon\dot{\psi}^2\cos\psi - M\varepsilon\ddot{\psi}\sin\psi + \sum_{i=1}^{n} m_i\{\ddot{X} - R(\ddot{\psi} + \ddot{\phi}_i)\sin(\psi + \phi_i) \\ - R(\dot{\psi} + \dot{\phi}_i)^2\cos(\psi + \phi_i)\} + k_X X = -c_X \dot{X}. \end{aligned} \tag{10}$$

The second equation of motion is

$$\begin{aligned} M\ddot{Y} - M\varepsilon\dot{\psi}^2\sin\psi + M\varepsilon\ddot{\psi}\cos\psi + \sum_{i=1}^{n} m_i\{\ddot{Y} + R(\ddot{\psi} + \ddot{\phi}_i)\cos(\psi + \phi_i) \\ - R(\dot{\psi} + \dot{\phi}_i)^2\sin(\psi + \phi_i)\} + k_Y Y + Mg + \sum_{i=1}^{n} m_i g = -c_Y \dot{Y}. \end{aligned} \tag{11}$$

The third equation of motion is

$$\begin{aligned} I_z\ddot{\psi} - M\varepsilon\ddot{X}\sin\psi + M\varepsilon\ddot{Y}\cos\psi + M\varepsilon^2\ddot{\psi} \\ - \sum_{i=1}^{n} m_i\{R[\ddot{X}\sin(\psi + \phi_i) - \ddot{Y}\cos(\psi + \phi_i)] + R^2(\ddot{\psi} + \ddot{\phi}_i)\} \\ + \sum_{i=1}^{n} m_i g R\cos(\psi + \phi_i) = \tilde{M}. \end{aligned} \tag{12}$$

Finally, the equation of motion of the ith ball is

$$-m_i R[\ddot{X}\sin(\psi + \phi_i) - \ddot{Y}\cos(\psi + \phi_i)] + m_i R^2(\ddot{\psi} + \ddot{\phi}_i) + m_i g R\cos(\psi + \phi_i) = -D_i\dot{\phi}_i. \tag{13}$$

Eqs. (10)–(13) can be simplified by assuming that all balls in the balancer have equal mass m, exert equal viscous drag D, and that the system is controlled not by a torsional load, but is forced to rotate at a constant angular velocity ω, that is,

$$m_i = m, \quad D_i = D, \quad \psi = \omega t, \quad i = 1 \ldots n. \tag{14}$$

The assumption of a constant angular velocity of the rotor, that is, acceleration effects are neglected, can be justified by envisaging a clamping mechanism in which the balls are fixed (providing a static initial condition in

the rotating frame) until the desired rotor speed is reached. Clamping mechanisms were first considered as practical devices in Refs. [8,18]. Note that from a practical point of view, the balls should be clamped in a symmetric configuration, for example, directly opposite one another in the case of two balls, so that they do not add to the eccentricity of the rotor during the acceleration phase.

2.2. Non-dimensionalisation

Eqs. (10)–(13), together with assumptions (14), can be written in dimensionless form by considering the non-dimensional states $\bar{X}$ and $\bar{Y}$, and the non-dimensional time $\bar{t}$, given by

$$\bar{X} = \frac{X}{R}, \quad \bar{Y} = \frac{Y}{R}, \quad \bar{t} = \omega_n t. \tag{15}$$

Furthermore, we introduce the dimensionless parameters

$$\mu = \frac{m}{M}, \quad \Omega = \frac{\omega}{\omega_n}, \quad \delta = \frac{\varepsilon}{R}, \quad G = \frac{g}{\varepsilon\omega_n^2}, \tag{16}$$

where ω_n is the natural frequency of the rotating disc, given by

$$\omega_n = \sqrt{\frac{k}{M}}. \tag{17}$$

Note that, to obtain this form for ω_n, and in the ensuing analysis, we will assume isotropic suspension of the rotor, that is,

$$\{c, k\} = \{c_X, k_X\} = \{c_Y, k_Y\}. \tag{18}$$

Finally, we introduce the remaining dimensionless parameters

$$\zeta = \frac{c}{2\sqrt{kM}}, \quad \beta = \frac{D}{mR^2\omega_n}, \tag{19}$$

describing the damping ratio of the rotor system ζ, and the non-dimensional viscous damping acting on the balls in the balancer β. Note that all the parameters are assumed to be positive. This is without loss of generality since negative ε implies an eccentric centre of mass on the negative axis, which can be mapped back to the positive axis by a simple change of coordinate frame.

Consequently, assuming Eq. (14), the rate equations (10), (11) and (13) can be written in the following dimensionless form:

$$(1+n\mu)\ddot{X} + 2\zeta\dot{X} + X = \delta\Omega^2\cos\Omega t + \mu\sum_{i=1}^{n}[\ddot{\phi}_i\sin(\Omega t+\phi_i) + (\Omega+\dot{\phi}_i)^2\cos(\Omega t+\phi_i)], \tag{20}$$

$$(1+n\mu)\ddot{Y} + 2\zeta\dot{Y} + Y = \delta\Omega^2\sin\Omega t - \mu\sum_{i=1}^{n}[\ddot{\phi}_i\cos(\Omega t+\phi_i) - (\Omega+\dot{\phi}_i)^2\sin(\Omega t+\phi_i) - G(1+n\mu)], \tag{21}$$

$$\ddot{\phi}_i - \ddot{X}\sin(\Omega t+\phi_i) + \ddot{Y}\cos(\Omega t+\phi_i) + \delta G\cos(\Omega t+\phi_i) = -\beta\dot{\phi}_i. \tag{22}$$

Note that, for simplicity, we drop the 'bar' notation used in Eq. (15). Furthermore, as we are not interested in the variation of the moment $\tilde{M}$, necessary to drive the system at a constant angular velocity ω, we do not consider the third equation of motion (12).

2.3. Autonomous equations in the rotating frame

The final part of our formulation converts the non-dimensional equations (20)–(22) to autonomous equations in a rotating frame of reference with constant angular velocity Ω [12,13]. This autonomous form is necessary in order to perform a full nonlinear bifurcation analysis using continuation techniques. To this end,

we consider the following substitutions:

$$X = x\cos(\Omega t) - y\sin(\Omega t), \tag{23}$$

$$Y = x\sin(\Omega t) + y\cos(\Omega t). \tag{24}$$

Furthermore, we ignore the effects of gravity, that is, we set $G = 0$ in Eq. (22). This assumption is justified because, in practice and for high rotation speeds, the centrifugal forces are much greater than the gravitational effect on the balls. Gravity can be neglected if the rotor is held in a horizontal position. Considering these assumptions results in the following autonomous dynamical system

$$\begin{pmatrix} 1+n\mu & 0 \\ 0 & 1+n\mu \end{pmatrix}\begin{pmatrix} \ddot{x} \\ \ddot{y} \end{pmatrix} + \begin{pmatrix} 2\zeta & -2\Omega(1+n\mu) \\ 2\Omega(1+n\mu) & 2\zeta \end{pmatrix}\begin{pmatrix} \dot{x} \\ \dot{y} \end{pmatrix} + \begin{pmatrix} K & -2\Omega\zeta \\ 2\Omega\zeta & K \end{pmatrix}\begin{pmatrix} x \\ y \end{pmatrix}$$
$$= \begin{pmatrix} \delta\Omega^2 \\ 0 \end{pmatrix} + \mu\sum_{i=1}^{n}\begin{pmatrix} (\Omega+\dot{\phi}_i)^2 & \ddot{\phi}_i \\ -\ddot{\phi}_i & (\Omega+\dot{\phi}_i)^2 \end{pmatrix}\begin{pmatrix} \cos\phi_i \\ \sin\phi_i \end{pmatrix} \tag{25}$$

and

$$\ddot{\phi}_i + \beta\dot{\phi}_i = (\ddot{x} - \Omega^2 x - 2\Omega\dot{y})\sin\phi_i - (\ddot{y} - \Omega^2 y + 2\Omega\dot{x})\cos\phi_i, \tag{26}$$

where $i = 1,\ldots,n$, and

$$K = 1 - \Omega^2(1+n\mu). \tag{27}$$

We note that by setting the right-hand side of Eq. (25) equal to zero we recover the equations of motion of a damped, isotropic rotor in the rotating frame. Similarly, setting $n = 0$, reduces Eq. (25) to the equations of motion for the Jeffcott rotor [19,20]. The consequence of the ADB is to add extra forcing terms provided by the motion of the balls.

3. Steady-state bifurcation analysis

In this section we consider the stability of the steady-state solutions of Eqs. (25) and (26). Specifically, in Section 3.1 we obtain the steady-state solutions, noting various conditions governing their existence, and in Section 3.2 we use the continuation package AUTO to compute bifurcation diagrams showing boundaries of stability in various parameter planes. For ease of presentation, in the analysis that follows, we study a system with two correction masses, that is, we set $n = 2$ in Eq. (25). The results are easily extended to the case of three or more balls.

3.1. Steady-state solutions

Steady-state solutions are obtained by setting all time derivatives in Eqs. (25) and (26) to zero. A balanced steady state occurs when the centre of mass of the system is at the origin, which from Eqs. (25) and (26) gives

$$\begin{aligned} &x = y = 0, \\ &\phi_1 = \arccos\left(-\frac{\delta}{2\mu}\right), \\ &\phi_2 = -\phi_1. \end{aligned} \tag{28}$$

In what follows, we will refer to Eq. (28) as the *balanced state* **1**.

There are two forms of steady-state solutions which are out of balance. Both of these solutions are given by $x, y \neq 0$. In this case, Eq. (26) gives us that

$$\frac{y}{x} = \tan\phi_i, \quad i = 1,2, \tag{29}$$

with solutions

$$\phi_1 = \phi_2 + k\pi. \tag{30}$$

Our first out of balance steady state corresponds to $k = 0$, that is, the two balls coincide (recall that we do not model collisions or interaction between the balls). Solutions, in terms of ϕ_1, are

$$x = \frac{K\Omega^2(2\mu\cos\phi_1 + \delta) + 4\mu\Omega^3\zeta\sin\phi_1}{K^2 + (2\Omega\zeta)^2},$$
$$y = \frac{2K\mu\Omega^2\sin\phi_1 - 2\Omega\zeta(\delta\Omega^2 + 2\mu\Omega^2\cos\phi_1)}{K^2 + (2\Omega\zeta)^2}, \tag{31}$$

where

$$\phi_1 = \pm\arccos\left(\frac{-4\mu\Omega\zeta}{\delta\sqrt{K^2 + (2\Omega\zeta)^2}}\right) - \arctan\left(\frac{-K}{2\Omega\zeta}\right),$$
$$\phi_2 = \phi_1. \tag{32}$$

In what follows, we will refer to Eqs. (31) and (32) as the *coincident state* $\mathbf{2}^{\pm}$.

Our second out of balance steady state corresponds to $k = 1$ in Eq. (30). That is, the balls are on opposite sides, and in line with the centre of rotation C. In this case,

$$x = \frac{\delta K\Omega^2}{K^2 + (2\Omega\zeta)^2},$$
$$y = \frac{-2\delta\Omega^3\zeta}{K^2 + (2\Omega\zeta)^2},$$
$$\phi_1 = \arctan\left(\frac{-2\Omega\zeta}{K}\right),$$
$$\phi_2 = \phi_1 + \pi. \tag{33}$$

In what follows, we will refer to Eq. (33) as the *in-line state* **3**.

Note that there are various conditions governing the existence of these steady-state solutions. The balanced state **1** given by Eq. (28) exists provided

$$\mu \geqslant \mu_c := \frac{\delta}{2}. \tag{34}$$

This means that, in order to achieve dynamic balance, the mass of the balls must be large enough to cope with the dimensionless eccentricity δ. Note that at the parameter values where equality is reached in Eq. (34), $\phi_1 = \pi$, $\phi_2 = -\pi$. This also corresponds to a coincident state $\mathbf{2}^{\pm}$ where both balls lie directly opposite to the imbalance. For $\mu < \delta/2$ state **1** ceases to exist, that is, it is destroyed when the balls become coincident. This is typical of a pitchfork bifurcation as we will see in Section 3.2.

The two coincident states $\mathbf{2}^{\pm}$ exist provided the modulus of the argument of the inverse cosine of Eq. (32) is less than unity, that is,

$$K^2 > (2\Omega\zeta)^2\left(\left(\frac{2\mu}{\delta}\right)^2 - 1\right). \tag{35}$$

This implies that for $\mu < \mu_c$ the coincident states $\mathbf{2}^{\pm}$ always exist.

In contrast, if $\mu > \mu_c$, we note that for both small Ω and in the limit $\Omega \to \infty$ the discriminant is positive. However, for an intermediary value of Ω, specifically at $\Omega = 1/\sqrt{1 + 2\mu}$, at which point K given by Eq. (27) vanishes, the discriminant is negative. Hence we have existence of the two coincident states $\mathbf{2}^{\pm}$ for small Ω which meet and disappear at some value Ω_{c1}, only to reappear at some higher Ω_{c2}. The values $\Omega_{c1,c2}$

depend on δ, ζ and μ in a nontrivial way. This is typical of a saddle-node bifurcation, and is confirmed as such in Section 3.2.

Finally, the in-line state **3**, given by Eq. (33), exists for all values of the physical parameters. Note that, like the balanced state **1**, it comes in two equivalent forms, obtained by exchanging ϕ_1 and ϕ_2. However, physically these correspond to the same state since the balls are assumed identical.

3.2. Numerical bifurcation diagrams

In this section, we use numerical bifurcation theory, specifically the continuation package AUTO [15], to investigate the stability of the steady states derived in Section 3.1, upon variation of parameters. Recall that we refer to the balanced equilibrium (28) as state **1**, and the coincident equilibria (31) as states $\mathbf{2}^{\pm}$, with the signs + or − corresponding to the two solutions of Eq. (32). In Ref. [12] a linear stability analysis of these solutions was performed using an ad hoc implementation of the Routh-Hurwitz criterion in a scatter-gun approach to search for boundaries between stability and instability. Our method is more general as it allows one to trace the precise linear stability boundaries (up to computational accuracy) via numerical bifurcation theory, and to determine whether these instabilities are oscillatory or static. Oscillatory instabilities (Hopf bifurcations) occur when a pair of pure eigenvalues cross the imaginary axis, and static bifurcations (either saddle-node bifurcations or pitchfork bifurcations) occur when a real eigenvalue passes through zero; see, for example, Refs. [21,22] for further details. We present results for the parameter regime investigated in Ref. [12]. However, our method can be applied to any other physically significant parameter set.

Figs. 2(a) and (b) show the results of a two-parameter bifurcation analysis upon variation of the dimensionless parameters Ω and μ, while considering the fixed parameters

$$\beta = \delta = \zeta = 0.01. \tag{36}$$

Physically, this corresponds to a small eccentricity and low damping in the suspension and balancing systems. Dashed lines in Figs. 2(a) and (b) correspond to Hopf bifurcations H, and solid lines to pitchfork bifurcations PF or saddle-node bifurcations SN. The darker shaded region corresponds to a stable balanced state **1**, light shading to stable coincident states $\mathbf{2}^{\pm}$, and no shading to a region where there are no stable steady-state solutions. Furthermore, in Fig. 2(a), the subscripts indicate which states are involved in the bifurcations and in Fig. 2(b) the subscripts indicate whether the states are stable (s) or unstable (u).

Figs. 2(c) and (d) show one-parameter bifurcation diagrams corresponding to vertical transitions through Figs. 2(a) and (b) for $\Omega = 0.5$ and 1.5, respectively. Stable steady states are drawn as solid lines, unstable as dashed lines. Pitchfork bifurcations PF are marked by a ($\times$) and Hopf bifurcations H are marked by a ($*$).

For the parameter values under consideration, the in-line state **3** was always found to be unstable and therefore of little physical interest. While it undergoes a Hopf bifurcation, the bifurcating steady state is already unstable (with one unstable eigenvalue), therefore so is the bifurcating periodic solution. The ensuing curve of Hopf bifurcations cuts through the middle of the parameter region in question, but does not interact with any other bifurcation curve and is therefore omitted from Fig. 2 for ease of presentation.

Fig. 2(a) shows that for $\mu < \mu_c = 0.005$ the only stable steady state is the coincident state $\mathbf{2}^{+}$. This solution is unstable inside the region bounded by the Hopf bifurcation H_{2+}. The coincident state $\mathbf{2}^{-}$ exists, but is always unstable for $\mu < \mu_c$; see Fig. 2(b).

For $\mu > \mu_c$ the balanced state **1** always exists. For small values of Ω the coincident state $\mathbf{2}^{+}$ is stable while the coincident state $\mathbf{2}^{-}$ is unstable; see Fig. 2(b). These steady states are born in a saddle-node bifurcation at the left-most boundary of the wedge-shaped region bounded by the curves $\mathrm{SN}_{2\pm}$. Inside this region the discriminant in Eq. (32) is negative and consequently, the coincident states $\mathbf{2}^{\pm}$ do not exist. The coincident states $\mathbf{2}^{\pm}$ reappear at the saddle-node bifurcation $\mathrm{SN}_{2\pm}$ forming the right-most boundary of this wedge. In this case, both states $\mathbf{2}^{\pm}$ are unstable; state $\mathbf{2}^{+}$ has three unstable eigenvalues while state $\mathbf{2}^{-}$ has one unstable eigenvalue. Note that the left and right boundaries of the wedge-shaped region correspond, respectively, to the critical points Ω_{c1} and Ω_{c2} identified at the end of Section 3.1. For increasing values of Ω, the unstable coincident state $\mathbf{2}^{+}$ undergoes a further Hopf bifurcation at the curve H_{2+}. Finally, for large values of Ω the balanced state **1** stabilises in a Hopf bifurcation H_1. Note that, for sufficiently large values of μ there are also a pair of Hopf bifurcations H_1 that stabilise the balanced state **1** around the *critical rotation speed* $\Omega = 1$.

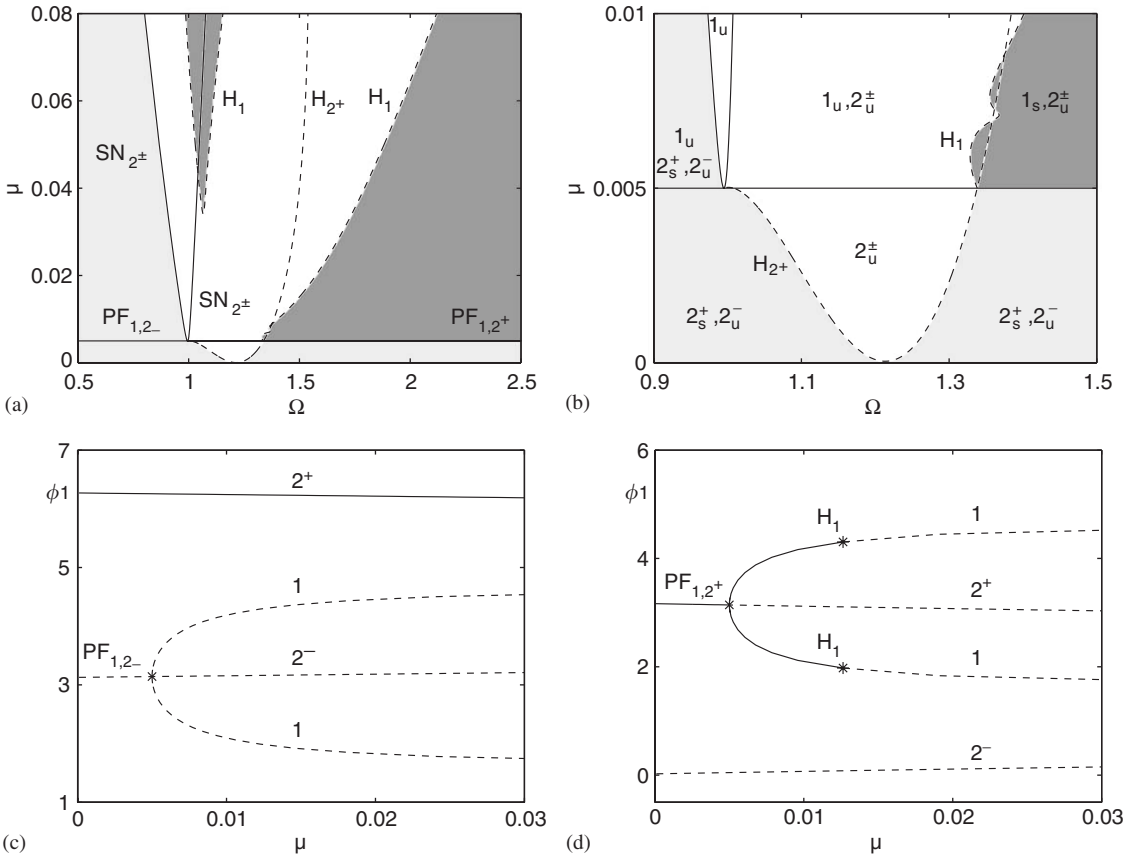

Fig. 2. Bifurcation diagrams of steady-state solutions showing curves of saddle-node SN, pitchfork PF, and Hopf bifurcations H in the (Ω, μ)-plane for $\beta = \delta = \zeta = 0.01$, (a) and (b). The subscripts indicate the bifurcating steady states. Dark shading corresponds to a stable balanced state **1**, and light shading to a stable coincident state $\mathbf{2}^+$. In panel (b), regions in which states **1** or $\mathbf{2}^\pm$ exist are shown to be stable ('*s*') or unstable ('*u*'). Panels (c) and (d) show one-parameter bifurcation diagrams in μ for $\Omega = 0.5$ and 1.5, respectively.

Fig. 2(b) shows that the curve of Hopf bifurcations H_{2^+} terminates at the low-Ω end in a codimension-two pitchfork-Hopf point [22] which is given precisely by

$$(\mu, \Omega) = (\mu_c, \Omega_c) := (\delta/2, 1/\sqrt{1+2\mu}) = (0.005, 0.9950372). \tag{37}$$

The point Ω_c also marks the tip of the wedge-shaped region bounded by the curves $SN_{2^\pm}$, that is, where the critical points Ω_{c1} and Ω_{c2} come together. Moreover, Ω_c is defined by $K = 0$ which is the analogue of the critical rotation speed $\Omega = 1$ in the case without the balancing mechanism ($\mu = 0$). For increasing values of Ω, the curve H_{2^+} meets the curve $PF_{1,2^+}$ again, at another codimension-two pitchfork-Hopf point given by $(\mu, \Omega) = (\mu_c, 1.338096)$; see Fig. 2(b).

The one-parameter bifurcation diagrams of Figs. 2(c) and (d) show the result of increasing μ through μ_c for $\Omega < \Omega_c$ and $\Omega > \Omega_c$, respectively. In both cases, the balanced state **1** is born in a pitchfork bifurcation PF from one of the coincident states $\mathbf{2}^\pm$. Note that the two copies of the balanced state **1** born in this bifurcation come from taking $\phi_1 \leftrightarrow \phi_2$. For $\Omega < \Omega_c$, see Fig. 2(c), it is the unstable coincident state $\mathbf{2}^-$ that is involved, creating an unstable balanced state **1**. As Ω is increased through Ω_c the roles of the coincident states $\mathbf{2}^-$ and $\mathbf{2}^+$ are reversed, but the balanced state **1** created is still unstable. As Ω is increased further through the second codimension-two pitchfork-Hopf bifurcation at $\Omega = 1.338096$, the pitchfork bifurcation PF changes in character again; see Fig. 2(d). It becomes supercritical so that the coincident state $\mathbf{2}^+$ and the bifurcating balanced state **1** are both stable. The balanced state **1** remains stable up to large values of Ω in our region of interest.

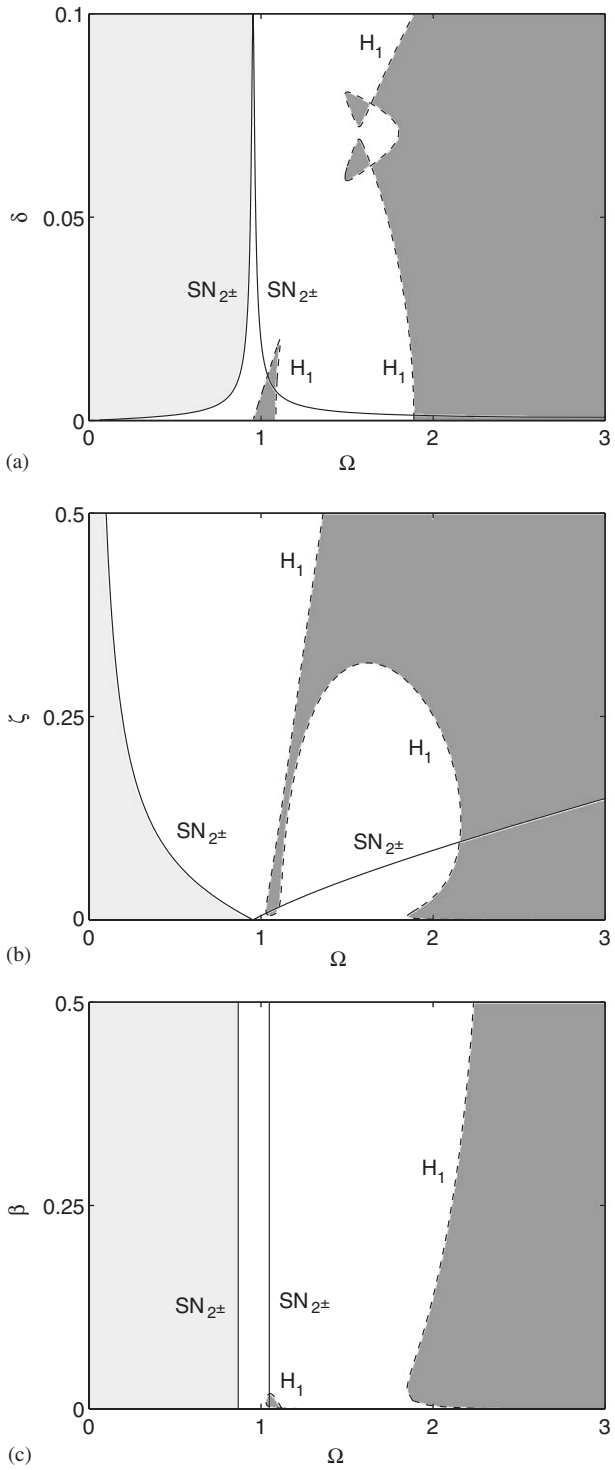

Fig. 3. Two-parameter bifurcation diagrams of steady-state solutions, showing saddle-node bifurcations of the coincident states $\mathbf{2}^{\pm}$ (solid lines) and Hopf bifurcations of the balanced state **1** (dashed line). Dark shaded regions correspond to a stable state **1** and light shaded regions to a stable state $\mathbf{2}^{+}$. When fixed, the parameters are $\mu = 0.05$, and $\beta = \delta = \zeta = 0.01$. The varying parameters are δ versus Ω (a), ζ versus Ω (b), and β versus Ω (c).

Now let us consider some stability diagrams akin to Fig. 2 in which we vary other dimensionless parameters. Henceforth, we shall assume that $\mu \geqslant \mu_c$ so that condition (34) needed for balance is satisfied.

Fig. 3 shows further two-parameter bifurcation analyses upon variation of other, physically relevant parameters. Specifically, Figs. 3(a)–(c) show dependence of stability boundaries upon variation of the dimensionless parameters controlling the eccentricity δ, the damping ratio of the rotor ζ, and the damping of the balls β, respectively, as the rotation speed Ω is increased. In each case, the onset of instability of the coincident states $\mathbf{2}^{\pm}$ appears in a saddle-node bifurcation $SN_{2^{\pm}}$, and the stability of the balanced state **1** in a Hopf bifurcation H_1. The same broad trends as in Fig. 2 are observed, namely that the coincident state $\mathbf{2}^{+}$ is stable for low enough values of Ω, whereas the balanced state **1** is stable for sufficiently large rotation speeds. In between is a region of instability where neither state is stable. Significantly, the onset of stability of the balanced state **1** is weakly sensitive to each of the system parameters, however it is always stable for $\Omega > 2.5$. Moreover, we note, from Figs. 3(a) and (b), that the details of what happens for intermediate values of Ω (between approximately 1.0 and 2.0) can be quite complex.

4. Limit cycle bifurcation analysis

The steady-state analysis of Section 3 suggests parameter regions where stable states exist. However, it does not address whether these constitute the only possible long-term behaviour at these parameter values. We also do not know what happens to the limit cycle oscillations which are born at the Hopf instabilities H_1.

In order to investigate the limit cycle solutions, we will consider the fixed parameter values

$$\zeta = \delta = \beta = 0.01, \quad \mu = 0.05 \tag{38}$$

and allow Ω to vary. This parameter set corresponds to a horizontal transition through Fig. 2(a). The value of μ is chosen such that there exist three Hopf bifurcations of the balanced state **1**. We are interested in the fate of each of the limit cycle oscillations born at these Hopf instabilities H_1. The results are plotted in Figs. 4–7.

Fig. 4(a) shows the stability of the steady-state solutions as Ω varies. Solid lines correspond to stable steady-state solutions and broken lines to unstable steady-state solutions. Furthermore, Hopf instabilities H_X are indicated by $(*)$, where the subscript X corresponds to the equilibrium state involved in the bifurcation. A saddle-node bifurcation SN is indicated by a $(\times)$.

Fig. 4(b) shows the branch of limit cycle solutions which emanate from the left-most Hopf bifurcation H_1 of Fig. 4(a) at $\Omega = 1.029697$. This branch is initially stable, that is, the Hopf bifurcation is supercritical. However, the Ω-interval of stability is very small; the branch is destabilised in a saddle-node bifurcation of limit cycles before the limit cycles reach large amplitude. The ensuing branch of unstable limit cycle solutions then undergoes a large sequence of period-doubling and fold bifurcations until it disappears at $\Omega \approx 0.984$. In fact, at this point, the period of the limit cycle approaches infinity; we will discuss this later.

The branch of limit cycle solutions emanating from the Hopf bifurcation H_1 at $\Omega = 1.093634$ is shown in Fig. 4(c). Again, the branch is initially stable but is quickly destabilised in a period-doubling bifurcation PD. Interestingly, this branch traces a global connection between the Hopf bifurcation H_1 of the balanced state **1** and one of the Hopf bifurcations H_3 of the in-line state **3**.

Finally, the branch emanating from the Hopf bifurcation H_1 at $\Omega = 1.882241$ is shown in Fig. 4(d). Again, this branch is initially stable but is quickly destabilised in a torus bifurcation T. Like the branch shown in Fig. 4(b), it undergoes a complicated sequence of bifurcations. In fact, in the results presented in Fig. 4(d) we do not reach any termination point despite the many twists and turns. Again, we note that there is an increase in the period of the solution along this branch.

Figs. 5(a) and (b) illustrate the long-term behaviour of the branches of limit cycle solutions emanating from the first and third Hopf bifurcations H_1, respectively. In Fig. 5(a) the branch is seen to 'cut-back' on itself so that the period does not increase monotonically. This is in contrast to the classic Shil'nikov 'wiggle' which is usually seen as the period of a branch tends to infinity and the limit cycle solutions bifurcate to homoclinic orbits [22]. This cut-back is more pronounced in the limit cycle branch shown in Fig. 5(b). As the period of the branch increases, the cut-backs are seen to decrease in size. Note that in Fig. 5(b) the branch will continue until, eventually the cut-backs are so small they form a vertical branch as in Fig. 5(a). This behaviour is reminiscent of curves of limit cycle solutions that have been found for Jeffcott rotors (our system without the

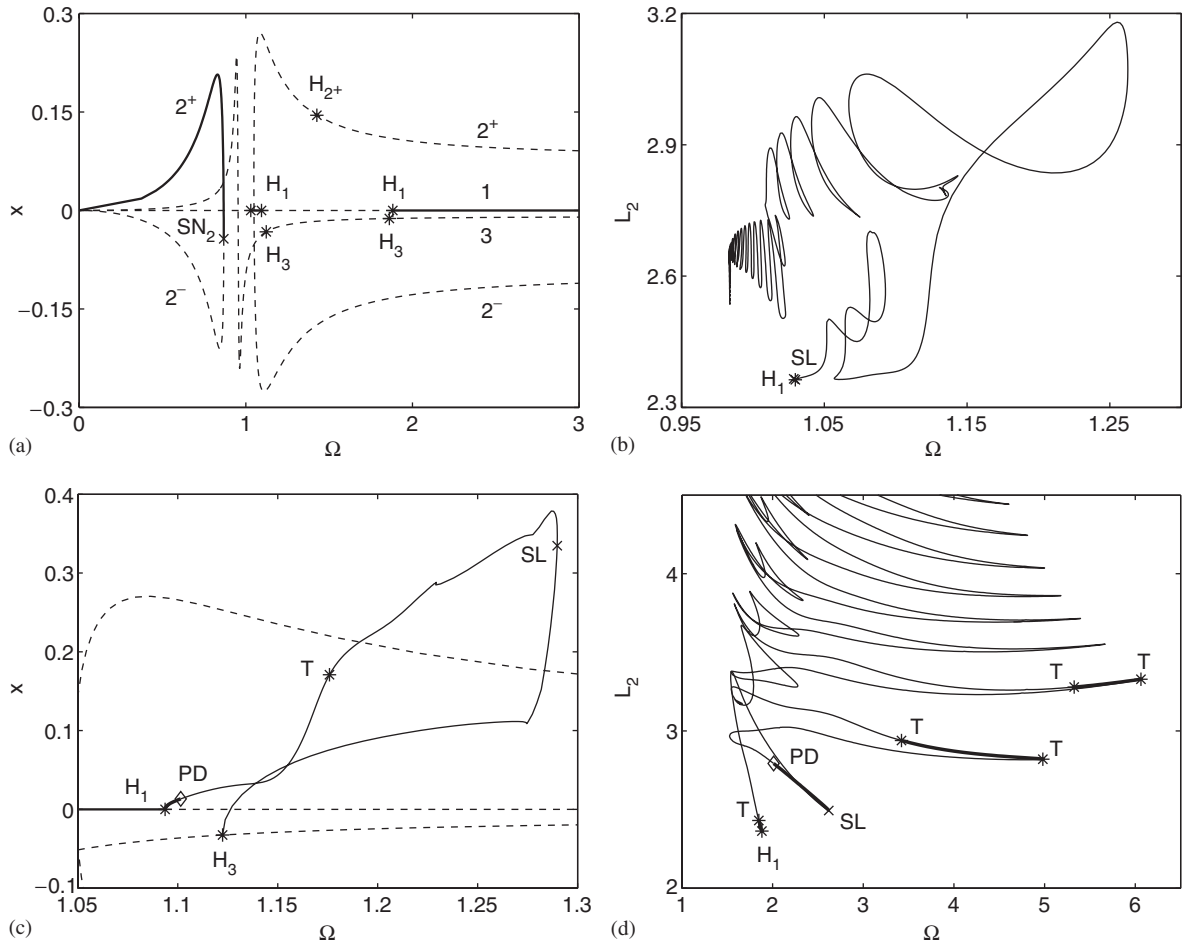

Fig. 4. One-parameter bifurcation diagrams showing a variation of Ω for $\zeta = \delta = \beta = 0.01$ and $\mu = 0.05$. Panel (a) shows stable states (solid line) and unstable states (dashed line). A saddle-node bifurcation is indicated by a ($\times$) and Hopf bifurcations H by a ($*$). Panels (b)–(d) show branches of stable (thick curve) and unstable (thin curve) limit cycles emanating from the three Hopf bifurcations H_1 of state **1**. Saddle-node bifurcations of limit cycles SL are indicated by a ($\times$), period-doubling bifurcations PD by a ($\diamond$) and torus bifurcations T by a ($*$). The ordinate L_2 represents the default norm used by AUTO, and x the maximum of the x-component.

ADB) close to the critical rotation speed $\Omega = 1.0$. The approach to a homoclinic bifurcation via these cutbacks is associated with a mechanism known as a *zipper* bifurcation, in which, upon variation of parameters, limit cycle solutions involved in mode-locking merge with a homoclinic bifurcation [23]. Physically, this can result in complicated rotor dynamics; for example, transitions from resonant behaviour and subharmonic vibrations to chaotic motion via period-doubling cascades [23].

Significantly, in Fig. 4(d) we identify four parameter intervals, in addition to the brief interval after the Hopf bifurcation H_1, in which the limit cycles are stable. These stable parameter regions are shown, together with steady-state stability, in Fig. 6. Fig. 7 shows representative limit cycles in projection onto the (x, y)-plane along the branch of solutions shown in Fig. 4(d). Fig. 7(a) shows an unstable limit cycle while Figs. 7(b)–(d) show limit cycles found on the stable parts of the branch; again see Fig. 6. Interestingly, the successive limit cycle solutions are seen to have an increasing number of loops in phase-space. Again, this is reminiscent of a zipper bifurcation; the closer Ω is to the homoclinic point the more loops occur [23]. Moreover, Fig. 6 shows that these stable oscillations coexist with the stable balanced state **1**. Hence it is clear that it is not enough to assert that a stable balanced equilibrium exists in order to have the successful operation of the ADB. One must determine whether the initial conditions are such that they are attracted to the balanced state **1** rather than to a limit cycle solution or to any other potentially stable, non-steady state.

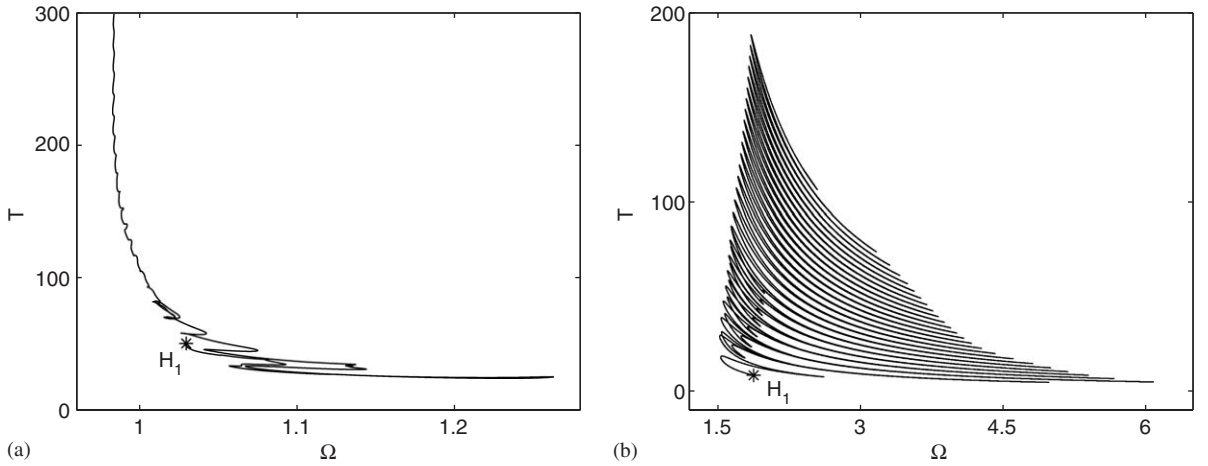

Fig. 5. Illustrating the long-term behaviour of the branches of limit cycle solutions shown in Figs. 4(b) and (d). Plotted is the period T (a) versus Ω (b).

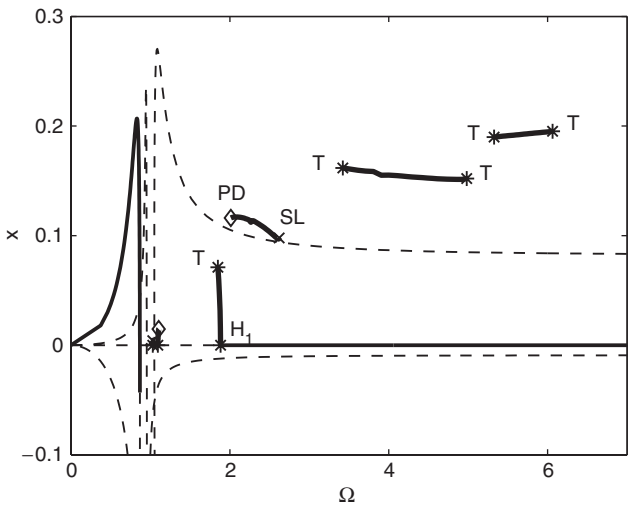

Fig. 6. One-parameter bifurcation diagrams showing the stable parts of the branches of limit cycles (indicated by thick curves) emanating from the Hopf bifurcations H_1; see Fig. 4. Note the bistability between stable limit cycles and the stable balanced state **1**.

These results have served to illustrate coexisting dynamical states. Other parameter sets can be similarly investigated, and a careful search can be made for other stable limit cycles quite possibly not connected to any Hopf bifurcation. However, such a further in-depth analysis might only be justified in order to try to match a physical parameter set for a particular experimental implementation of the ADB and is beyond the scope of this paper. Instead, through numerical simulation of the equations of motion, let us examine the bistabilities we have discovered.

5. Numerical simulation

We now present results obtained by direct numerical integration of the governing equations (25) and (26) derived in Section 2. In our experiments, we use the `Matlab` routine `ode45`. As a test, we note that our simulations agree with those of Ref. [12] at the four sets of parameter values they use (with fixed initial conditions).

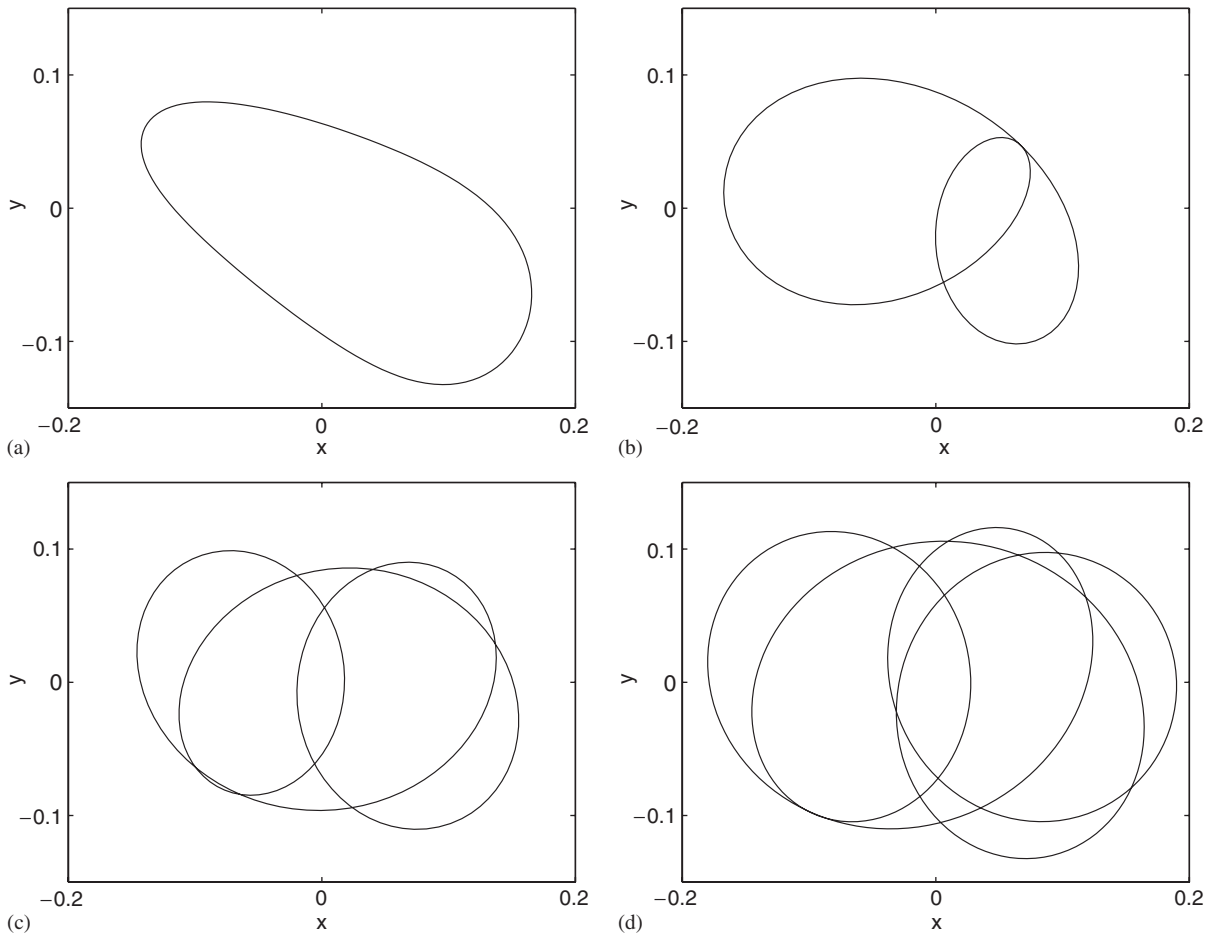

Fig. 7. Limit cycle solutions found along the branch shown in Fig. 4(d). Panel (a) shows an unstable limit cycle at $\Omega = 1.646937$, with period $\mathsf{T} = 12.57059$; panel (b) shows a stable limit cycle at $\Omega = 2.31867$ and $\mathsf{T} = 9.39826$; panel (c) shows a stable limit cycle at $\Omega = 4.00000$ and $\mathsf{T} = 6.21052$; and panel (d) shows a stable limit cycle at $\Omega = 5.32585$ and $\mathsf{T} = 5.75791$.

A large number of numerical runs were conducted for the parameter set (38) with $\Omega = 4.0$. This particular value of Ω was chosen since Fig. 6 identifies a coexistence between the stable balanced state **1** and a stable limit cycle oscillation. The results of taking key initial conditions are shown in Figs. 8 and 9. In both figures, we plot dimensionless time against both the amplitude of the radial vibration $r = \sqrt{(x^2 + y^2)}$ (where the black curve represents the motion of the rotor with the ADB and the grey curve the motion of the rotor without the ADB) and the angular position of the balls ϕ_1 (black curve) and ϕ_2 (grey curve). In general it was found there was little sensitivity to the initial position of the centre of rotation (x and y) or its velocity ($\dot{x}$ and $\dot{y}$). Therefore, all results depicted are for initial values of x, y, $\dot{x}$, $\dot{y}$ equal to zero. However, variation of the initial position of the balls (ϕ_1 and ϕ_2) and their respective velocities ($\dot{\phi}_1$ and $\dot{\phi}_2$) was found to produce a wide variation in the results.

Fig. 8 shows the result of taking initial conditions such that the balls are initially stationary (within the rotating frame) but are launched symmetrically opposite to each other such that the line joining them is orthogonal to the axis of eccentricity (the x-axis). Note that if the balls are clamped in this way during acceleration, they do not add to the rotor eccentricity. In other words, $x = y = \dot{x} = \dot{y} = \dot{\phi}_1 = \dot{\phi}_2 = 0$, $\phi_1 = -\pi/2$, and $\phi_2 = \pi/2$. Fig. 8(a) shows that after $t \approx 400$ balance is achieved. However, we note that the transient period for both the rotor with the ADB (black curve) and for the rotor without the ADB (grey curve) are approximately the same. Fig. 8(b) shows that the balls get attracted to the balanced state **1** with values of angular position $\phi_{1,2}$ given by Eq. (28).

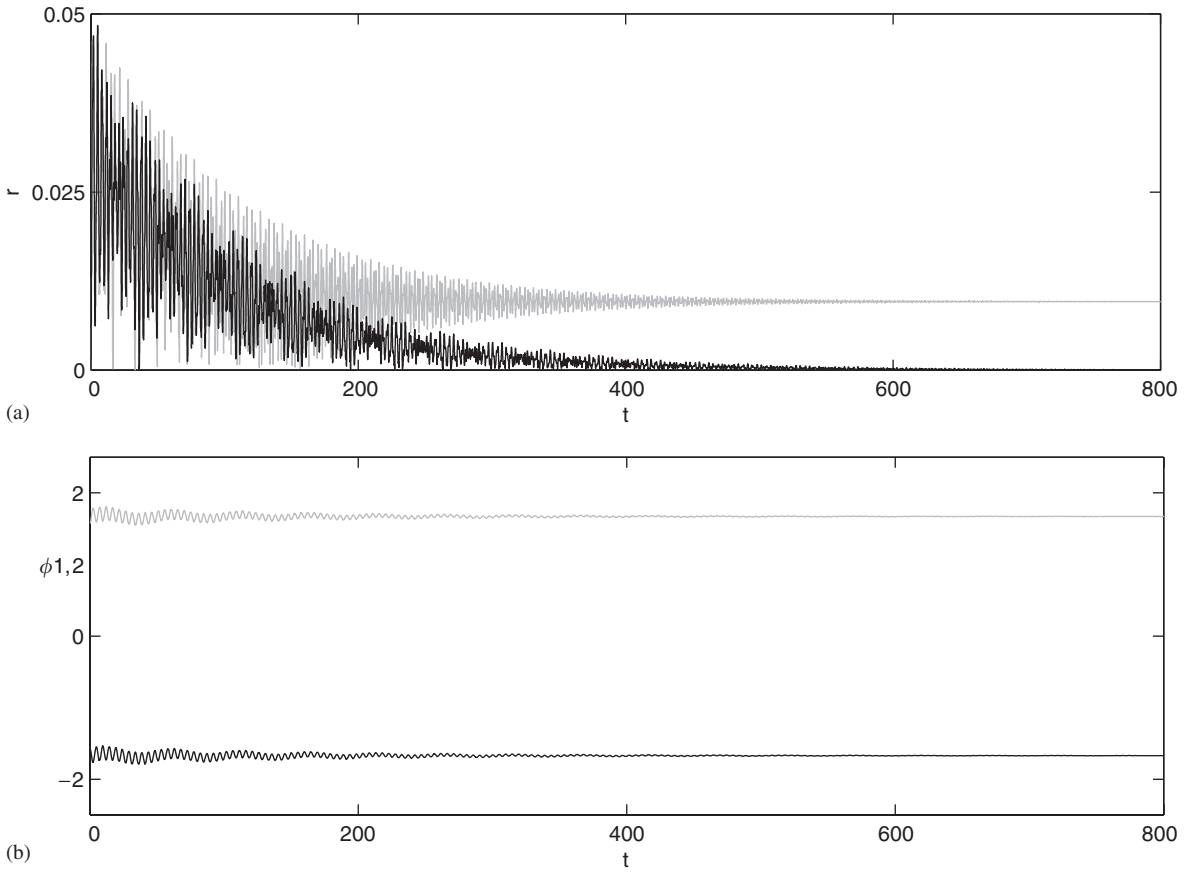

Fig. 8. Numerical simulations for the parameter set $\Omega = 4.0$, $\zeta = 0.01$, $\beta = 0.01$, $\delta = 0.01$, and $\mu = 0.05$. Panel (a) shows the radial vibration $r = \sqrt{x^2 + y^2}$, while panel (b) shows the ball positions $\phi_{1,2}$, against time t. Initial conditions were fixed at $x = y = \dot{x} = \dot{y} = \dot{\phi}_1 = \dot{\phi}_2 = 0$, $\phi_1 = -\pi/2$, and $\phi_2 = \pi/2$.

Fig. 9 shows simulations where initial conditions are attracted to limit cycle oscillations. Fig. 9(a) shows the result taking initial conditions $x = y = \dot{x} = \dot{y} = \dot{\phi}_1 = \dot{\phi}_2 = 0$, and $\phi_1 = 9\pi/32$, $\phi_2 = -9\pi/32$. The trajectory of the rotor system with the ADB (shown in black) is attracted to the limit cycle identified in Fig. 7(c). At these parameter values, Fig. 9(b) shows the balls oscillating about the coexisting balanced state **1**.

Finally, Figs. 9(c) and (d) show a second possible oscillatory behaviour, albeit a highly undesirable one from the point of view of trying to achieve dynamic balance. Here the balls are started at absolute rest, that is, with speed $\dot{\phi}_1 = -\Omega$ and $\dot{\phi}_2 = -\Omega$ within the rotating frame. The result is a periodic motion that is not captured by the above bifurcation analysis, since the ball ϕ_1 continues to rotate, rather than to oscillate about some fixed angle as it does in the limit cycles previously identified. Fig. 9(d) shows that the ball with position ϕ_2 (shown in grey) does cease to rotate and undergoes only small oscillations about some mean position. Note the offset and amplitude of the ensuing oscillations in r; see Fig. 9(c). The mean value of $r \approx 0.3$ is an order of magnitude worse that the eccentric motion without the ADB. However, we note that a clamping mechanism, ensuring that the balls are released with initial angular velocity equal to that of the rotor, would avoid such dynamics.

We now turn to investigating the effect which a variation of the dimensionless parameters has on the dynamics of the ADB. For all subsequent runs we used the same initial conditions as the runs which produced Fig. 8(a); namely

$$\begin{aligned} &x(0) = y(0) = \dot{x}(0) = \dot{y}(0) = 0, \\ &\phi_1 = -\pi/2, \quad \phi_2 = \pi/2, \quad \dot{\phi}_1 = 0, \quad \text{and} \quad \dot{\phi}_2 = 0. \end{aligned} \tag{39}$$

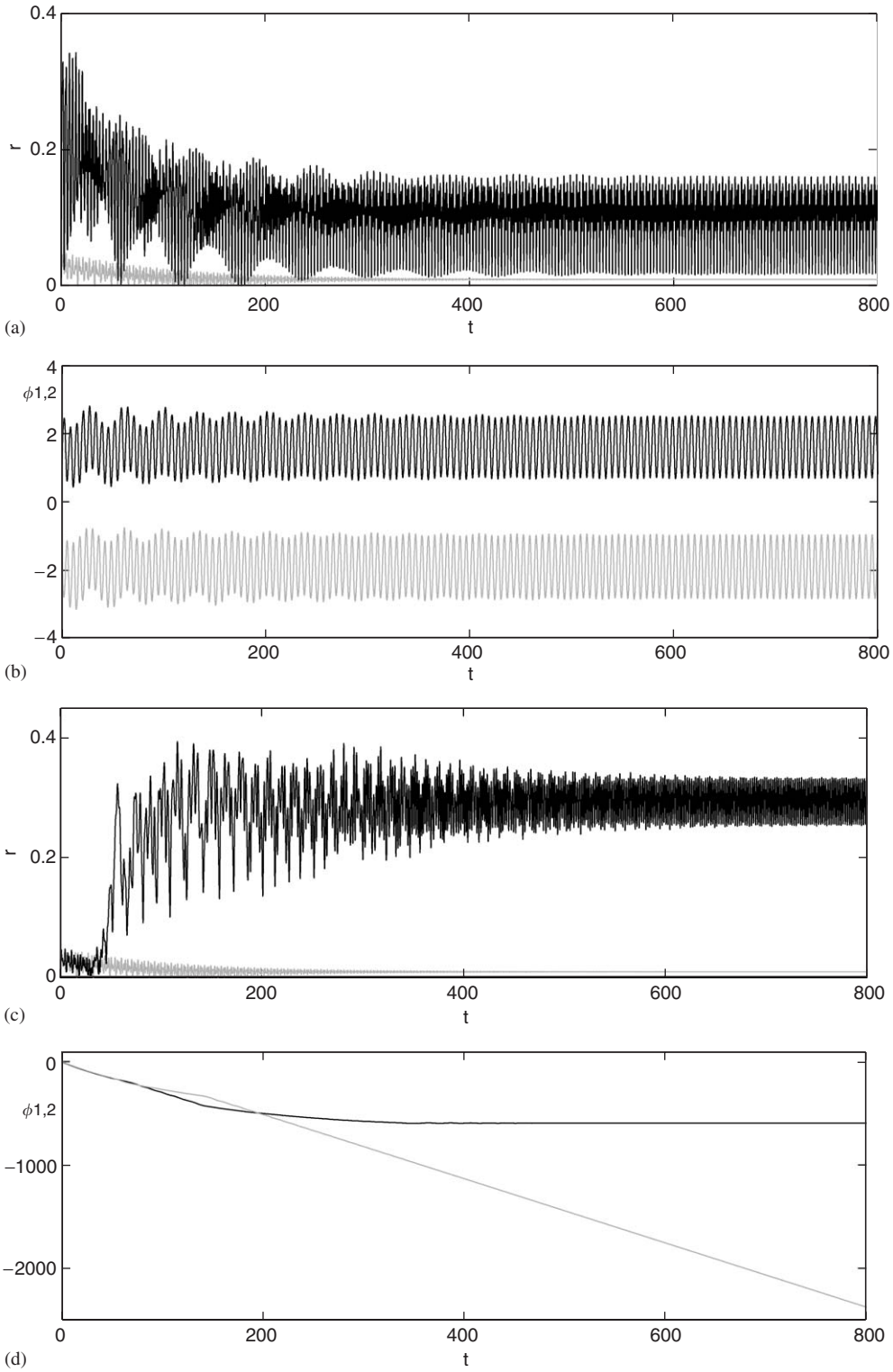

Fig. 9. Numerical simulations showing periodic oscillations for the parameter set $\Omega = 4.0$, $\zeta = 0.01$, $\beta = 0.01$, $\delta = 0.01$, and $\mu = 0.05$. Panels (a) and (c) show radial vibrations $r = \sqrt{x^2 + y^2}$, while panels (b) and (d) show ball positions $\phi_{1,2}$, against time t. Initial conditions were fixed at $x = y = \dot{x} = \dot{y} = \dot{\phi}_1 = \dot{\phi}_2 = 0$; and $\phi_1 = -\phi_2 = \pi/2$ (a) and (b), $\phi_1 = -\phi_2 = 9\pi/32$ (c) and (d).

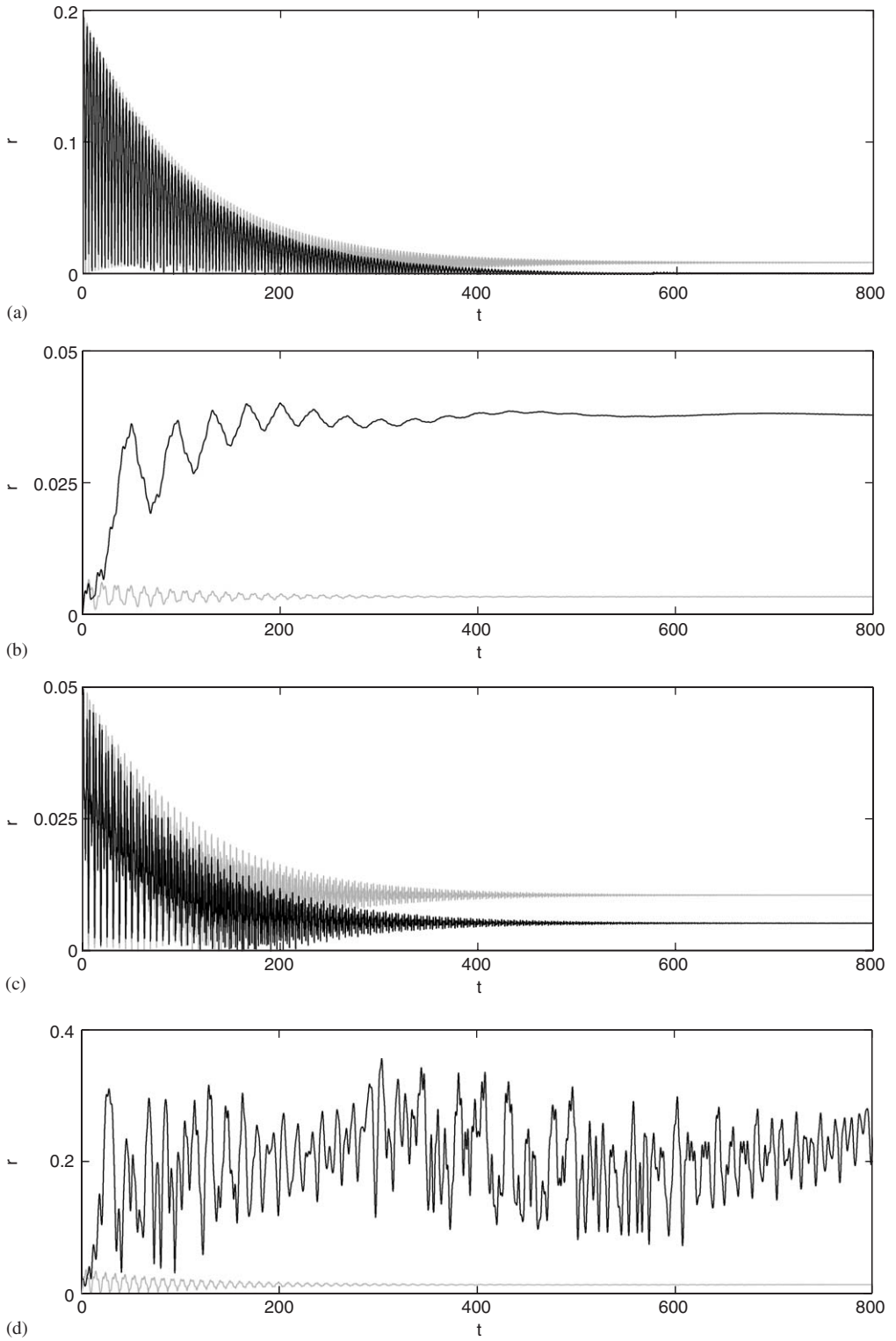

Fig. 10. Numerical simulations for the parameter set $\zeta = 0.01$, $\beta = 0.01$, and $\delta = 0.01$. Initial conditions were fixed at $x = y = \dot{x} = \dot{y} = \dot{\phi}_1 = \dot{\phi}_1 = 0$, $\phi_1 = -\pi/2$, and $\phi_2 = \pi/2$. Values of Ω and μ fixed at $(\Omega, \mu) = (20.0, 0.05)$ (a), $(0.5, 0.05)$ (b), $(4.0, 0.0025)$ (c), and $(1.6, 0.05)$ (d).

In other words, the balls were launched, with an angular velocity equal to that of the rotor, from positions symmetrically opposite to each other such that the line joining them was orthogonal to the axis of eccentricity.

Fig. 10 explores the dynamics of different regions of the bifurcation diagram shown in Fig. 2(a). Fig. 10(a) depicts a high-rotation speed $\Omega = 20.0$ and $\mu = 0.05$, this is well to the right of the stability boundary H_1 for the balanced state **1**; see Fig. 2(a). Balance is eventually achieved, albeit at the expense of a huge transient motion which has values of radial vibration up to $r \approx 0.2$. Fig. 10(b) shows the case for $\Omega = 0.5$ and $\mu = 0.05$. Eventually the transient of the rotor with the ADB (shown in black) becomes attracted to the stable coincident state $\mathbf{2}^+$, and the values of ϕ_1 and ϕ_2 (not depicted) are indeed observed to converge. However, for these parameter values, this steady state results in a much greater radial vibration r than would be the case without the ADB (shown in grey). Fig. 10(c) shows a case with a small mass ratio $\mu = 0.0025$ and $\Omega = 4.0$. This does not satisfy the balance condition (34) for the given eccentricity δ. Here, as predicted by the bifurcation analysis, the coincident state $\mathbf{2}^+$ is stable. In contrast to Fig. 10(b), this final state with the ADB (shown in black) is preferable to that obtained without the ADB (shown in grey). In fact, for $\mu < \mu_c$ (34), the coincident state is situated on the same side of the rotor as the imbalance for $\Omega < 1$, thus causing a greater radial vibration. However, as Ω is increased past resonance, the coincident state moves to the other side of the rotor, opposite to the imbalance, and a reduction in the radial vibration is observed. Fig. 10(d) depicts the case for $\Omega = 1.6$ and $\mu = 0.05$. Here the bifurcation analysis finds no stable equilibria (or limit cycles). The rotor with the ADB (shown in black) appears now to undergo chaotic motion, again reaching much larger values of radial vibration r than the rotor without the ADB mechanism.

Finally, Figs. 11 and 12 show brute force bifurcation diagrams obtained by simulation for varying values of Ω and varying initial positions of the balls $\phi_1(0)$ and $\phi_2(0)$. In both cases, other parameter values were fixed at

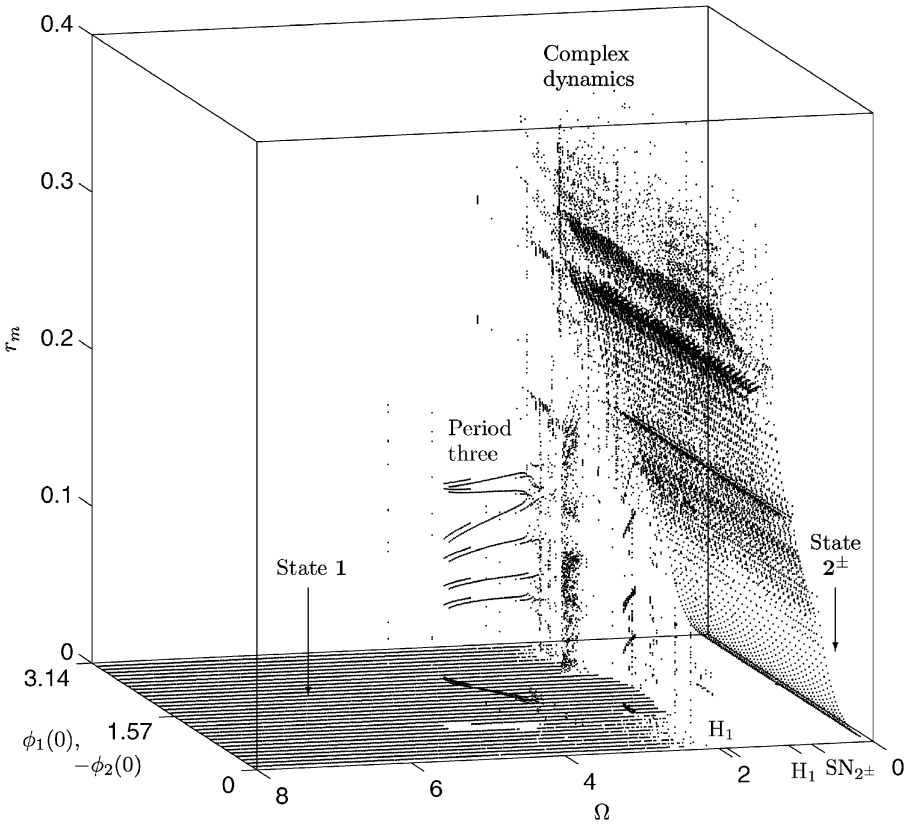

Fig. 11. Bifurcation diagram obtained by simulation showing the attracting dynamics for varying Ω and $\phi_1(0) = -\phi_2(0) \in [0, \pi]$. Parameters were fixed at $\mu = 0.05$, $\beta = \delta = \zeta = 0.01$, and initial conditions at $x(0) = y(0) = \dot{x}(0) = \dot{y}(0) = \dot{\phi}_1(0) = \dot{\phi}_2(0) = 0.0$; r_m represents the extrema of $r = \sqrt{(x^2 + y^2)}$ for each attracting solution. $SN_{2^{\pm}}$ indicates a saddle-node bifurcation of state $\mathbf{2}^{\pm}$ and H_1 a Hopf bifurcation of state **1**.

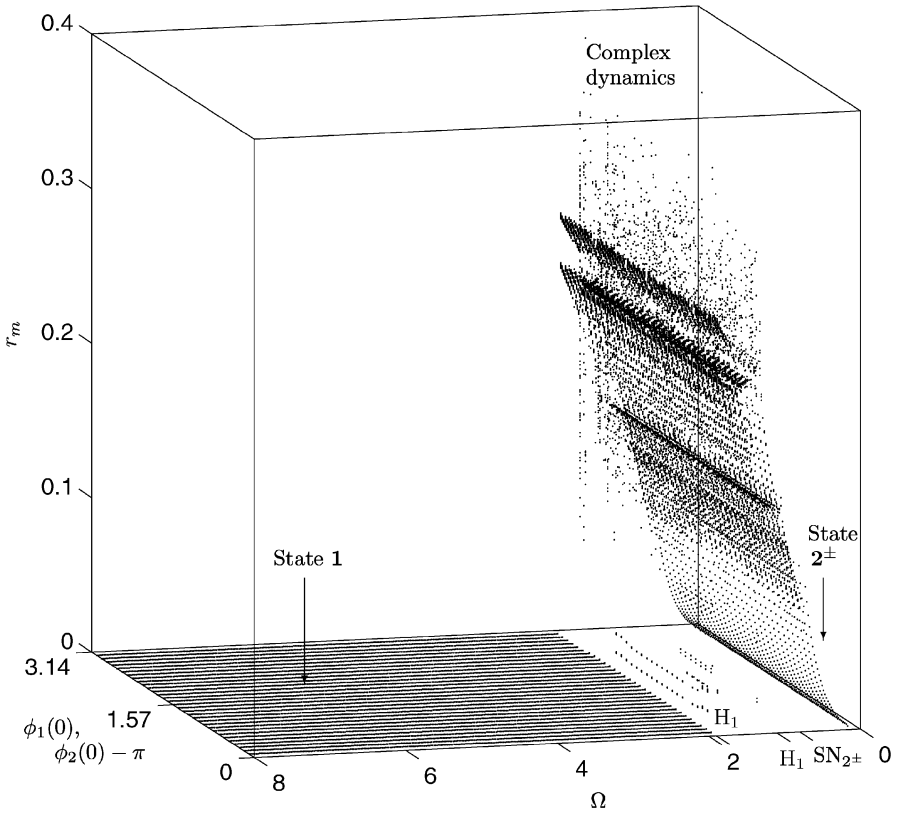

Fig. 12. Bifurcation diagram obtained by simulation showing the attracting dynamics for varying Ω and $\phi_1(0) = \phi_2(0) + \pi \in [0, \pi]$. Parameters were fixed at $\mu = 0.05$, $\beta = \delta = \zeta = 0.01$, and initial conditions at $x(0) = y(0) = \dot{x}(0) = \dot{y}(0) = \dot{\phi}_1(0) = \dot{\phi}_2(0) = 0.0$; r_m represents the extrema of $r = \sqrt{(x^2 + y^2)}$ for each attracting solution. $SN_{2^{\pm}}$ indicates a saddle-node bifurcation of state $\mathbf{2}^{\pm}$ and H_1 a Hopf bifurcation of state **1**.

$\mu = 0.05$, $\beta = \delta = \zeta = 0.01$, and initial conditions at $x(0) = y(0) = \dot{x}(0) = \dot{y}(0) = \dot{\phi}_1(0) = \dot{\phi}_2(0) = 0$. Each figure was computed as follows: for each value of Ω and for initial conditions $\phi_1(0)$ and $\phi_2(0)$ we let transients die away and plotted the minimum and maximum values r_m of the amplitude of the radial vibration $r = \sqrt{(x^2 + y^2)}$ of the attracting solution. Specifically, for Fig. 11 we used 'symmetric' initial conditions $\phi_1(0) = -\phi_2(0) \in [0, \pi]$, and for Fig. 12 we used 'opposite' initial conditions $\phi_1(0) = \phi_2(0) + \pi \in [0, \pi]$. In this way, for fixed $\phi_1(0)$, $\phi_2(0)$ and Ω, a single point corresponds to a steady-state solution, a small number of points to a limit cycle solution and a large number of points to quasiperiodic or chaotic dynamics.

We first address the similarities between Figs. 11 and 12. As was shown in Fig. 2, the coincident state $\mathbf{2}^{\pm}$ is stable for low values of Ω. This equilibrium is destabilised in the saddle-node bifurcation $SN_{2^{\pm}}$ at $\Omega \approx 0.8$. For increasing values of Ω, the ensuing region of instability is shown to produce coexisting states of complex dynamics with large radial vibrations; as in Fig. 10(d). This would appear to include both dynamics that is truly chaotic and also high-period limit cycle solutions. Moreover, we observe a few points with $r = 0$ at $\Omega \approx 1.0$. This corresponds to the stable balanced state **1** enclosed by the wedge formed by the two Hopf bifurcations H_1; see Fig. 2. Furthermore, the balanced state **1** is stabilised in the second Hopf bifurcation H_1 at $\Omega \approx 1.9$.

The main difference between the two figures is that, in Fig. 11, and for $\Omega \in [1.9, 2.7]$, the balanced state **1** is shown to coexist with the complex dynamics. The complexity of these dynamics is reduced for $\Omega \in [2.7, 4.9]$ where we observe coexistence between the balanced state **1** and various attracting limit cycles, in particular we observe a large parameter window of period three motion. In this region of coexistence, the non-steady-state dynamics develop from balls launched with initial angles $\phi_1(0) = -\phi_2(0) \approx 9\pi/32$; see Figs. 9(a) and (b).

Finally, in Fig. 11, for $\Omega > 4.9$ the balanced state **1** is shown to be the only attracting solution for all initial conditions $\phi_1(0) = -\phi_2(0) \in [0, \pi]$.

Significantly, we see no such coexistence between the balanced state **1** and limit cycles solutions in Fig. 12. For values of $\Omega > 1.9$, irrespective of the position of the imbalance, if the balls are launched at directly opposite positions within the ball race, the system always reaches the balanced state **1**. Again, we note that balls clamped in opposite positions before release do not add to the eccentricity of the rotor during the acceleration phase. This is very promising and encourages further experimental investigation.

6. Conclusions

We have provided the first nonlinear bifurcation analysis of a two-ball automatic dynamic balancing mechanism for eccentric rotors. Two-parameter bifurcation diagrams obtained by continuation showed that dynamic balance can easily be achieved provided the ratio between the mass of the rotor system and the mass of each balancing ball μ is higher that half the eccentricity δ. This balanced state was shown to stabilise in a Hopf bifurcation for sufficiently high values of the rotation speed Ω.

Furthermore, even if the eccentricity is so great that balance is not ultimately achieved, due to low values of the ball mass in the balancer or if the rotation speed was not high enough, a coincident-ball equilibrium position was shown to be stable. Results by numerical simulation showed that, for low ball mass and large rotation speeds, this provided an improvement to the balance of the rotor without the ADB mechanism.

Continuation techniques were used to investigate the limit cycles emanating from the Hopf bifurcations. Our analysis showed that these stable solutions may coexist with the stable balanced equilibrium. Numerical simulations showed that the determination of which of the competing states is reached is highly sensitive to the initial position of the balls, and relatively insensitive to the initial position of the axis of the rotor.

Our investigations showed that, for the parameter region investigated, releasing the balls from positions symmetrically opposite to each other led to dramatic improvements in achieving balance; see Fig. 8. However, even in this case, the results in Fig. 11 show that there can be sensitive dependence on the angle at which the balls are released for intermediate rotation speeds, or when close to the critical rotation speed. Further improvement was observed when releasing the balls from directly opposite positions in the ball race. In fact, we observed no coexistence between the balanced state and other attracting dynamics at intermediate rotation speeds. Finally, our simulations showed that even if auto-balance is achieved, the initial transients may be large. This transient behaviour is investigated in detail in Ref. [24].

Clearly the non-steady-state dynamics play a crucial role in a complete understanding of this highly nonlinear mechanism. This paper has outlined a method of analysis based on numerical bifurcation theory combined with careful simulation. More work would be required, utilising the methods presented in this paper, in order to reach an optimal design for a particular physical application. This would clearly need to be tested against experiment.

References

[1] P.C.P. Chao, Y.-D. Huang, C.-K. Sung, Non-planar dynamic modeling for the optical disk drive spindles equipped with an automatic balancer, *Mechanism and Machine Theory* 38 (2003) 1289–1305.

[2] W.-Y. Huang, C.-P. Chao, J.-R. Kang, C.-K. Sung, The application of ball-type balancers for radial vibration reduction of high-speed optic drives, *Journal of Sound and Vibration* 250 (3) (2002) 415–430.

[3] W. Kim, J. Chung, Performance of automatic ball balancers on optical disc drives, *Proceedings of the Institution of Mechanical Engineers Part C: Journal of Mechanical Engineering Science* 216 (2002) 1071–1080.

[4] N. van de Wouw, M.N. van den Heuvel, J.A. van Rooij, H. Nijmeijer, Performance of an automatic ball balancer with dry friction, *Int. J. Bifurcation and Chaos* 15 (2005) 65–82.

[5] R. Rajalingham, S. Rakheja, Whirl suppression in hand-held power tool rotors using guided rolling balancers, *Journal of Sound and Vibration* 217 (3) (1998) 453–466.

[6] Health and Safety Executive, *Hand-arm Vibration*, vol. HS(G)88, HSE Books, Sudbury, 1994, ISBN 0-7176-0743-7.

[7] J. Lee, W.K. Van Moorhem, Analytical and experimental analysis of a self-compensating dynamic balancer in a rotating mechanism, *Transactions of the ASME* 118 (1996) 468–475.

[8] E. Thearle, A new type of dynamic-balancing machine, *Transactions of the ASME* 54 (APM54-12) (1932) 131–141.

[9] R.S. Sharp, An analysis of a self-balancing system for rigid rotors, *Journal of Mechanical Engineering Science* 17 (4) (1975) 186–189.

[10] P. Bövik, C. Högfors, Autobalancing of rotors, *Journal of Sound and Vibration* 111 (3) (1986) 429–440.
[11] T. Majewski, Synchronous vibration eliminator for an object having one degree of freedom, *Journal of Sound and Vibration* 112 (3) (1987) 401–413.
[12] J. Chung, D.S. Ro, Dynamic analysis of an automatic dynamic balancer for rotating mechanisms, *Journal of Sound and Vibration* 228 (5) (1999) 1035–1056.
[13] J. Adolfsson, Passive Control of Mechanical Systems: Bipedal Walking and Autobalancing, PhD Thesis, Royal Institute of Technology, Stockholm, 2001.
[14] SKF Autobalance Systems, Dynaspin, http://dynaspin.skf.com, 2000.
[15] E. Doedel, A. Champneys, T. Fairgrieve, Yu. Kuznetsov, B. Sandstede, X. Wang, AUTO 97: continuation and bifurcation software for ordinary differential equations, http://indy.cs.concordia.ca/auto/main.html, 1997.
[16] J. Chung, I. Jang, Dynamic response and stability analysis of an automatic ball balancer for a flexible rotor, *Journal of Sound and Vibration* 259 (1) (2003) 31–43.
[17] C.-H. Hwang, J. Chung, Dynamic analysis of an automatic ball balancer with double races, *JSME International Journal: Series C* 42 (2) (1999) 265–272.
[18] H. Ernst, Automatic Precision Balancing, Machine Design, January 1951.
[19] H.H. Jeffcott, The lateral vibration of loaded shafts in the neighbourhood of a whirling speed—the effect of want of balance, *Philosophical Magazine Series* 6 (37) (1919) 304–314.
[20] R.A. Zalik, The Jeffcott equations in nonlinear rotordynamics, *Quarterly of Applied Mathematics* 4 (1989) 585–599.
[21] J. Guckenheimer, P. Holmes, *Nonlinear Oscillations, Dynamical Systems, and Bifurcations of Vector Fields*, Springer, Berlin, 1983.
[22] Y. Kuznetsov, *Elements of Applied Bifurcation Theory*, Springer, Berlin, 1995.
[23] G.H.M. van der Heijden, Bifurcation sequences in the interaction of resonances in a model deriving from nonlinear rotordynamics: the zipper, *Dynamics and Stability of Systems* 15 (2000) 159–183.
[24] K. Green, A.R. Champneys, M.I. Friswell, Analysis of the transient response of an automatic balancer for eccentric rotors, International Journal of Mechanical Sciences (2005); in press.